

---

# AERODYNAMIC SIMULATION STRATEGIES ASSESSMENT FOR A FENESTRON® IN HOVER FLIGHT

---

M. Marino<sup>1,2</sup>, N. Gourdain<sup>3</sup>, G. Legras<sup>4</sup>, and D. Alfano<sup>4</sup>

<sup>1</sup>Airbus Helicopters SAS  
Marignane 13725, France

<sup>2</sup>CERFACS  
Toulouse 31057, France

<sup>3</sup>Department of Aerodynamics, Energetics and Propulsion  
ISAE Sup'Aero, Toulouse 31400, France

<sup>4</sup>Aerodynamics Department, Airbus Helicopters SAS  
Marignane 13725, France

The Fenestron® has a crucial antitorque function and its sizing is a key point of the Helicopter design, especially regarding thrust and power predictions. This paper reports the investigations done on a full scale Dauphin Fenestron®. The objectives are, first, to evaluate the influence of some numerical parameters on the performance of the Fenestron®; and then, the flow is analyzed for a high incidence pitch, for which the rotor blade can experience massive boundary layer separations. Simulations are carried out on a single blade passage model. Several parameters are benched such as grid quality, numerical schemes, and turbulence modeling. A comparison with test bench measurements is carried out to evaluate the capability of the numerical simulations to predict both global performance (thrust and power) and local flows (static pressure at the shroud and radial profiles inside the vein). The analysis demonstrates the capability of numerical simulations to accurately estimate the global performance of the Fenestron®, including at high pitch angles. However, some discrepancies remain on the local flow, especially in the vicinity of the rotor shroud. A more detailed analysis of the local flow is performed at a blade pitch angle of 35°, with a particular interest for the blade tip region.

## ABBREVIATIONS

ADT     Alternative Digital Trees  
AUSMP   Advection Upstream Splitting Method Preconditioned  
CFD     Computational Fluid Dynamics

elsA	ensemble logiciel de simulation en Aérodynamique
JST	Jameson–Schmidt–Turkel
L–S	Launder–Sharma
LES	Large Eddy Simulation
MUSCL	Monotone Upwind Scheme for Scalar Conservative Laws
RANS	Reynolds-Averaged Navier–Stokes
S–A	Spalart–Allmaras
SST	Shear Stress Transport

## NOMENCLATURE

CFP	Fenestron <sup>®</sup> power coefficient, $FP/(\rho\pi R^2 V_{\text{tip}}^3)$
CFT	Fenestron <sup>®</sup> thrust coefficient, $FT/(\rho\pi R^2 V_{\text{tip}}^2)$
$C_p$	Pressure coefficient, $(p - p_\infty)/(0.5\rho V_{\text{tip}}^2)$
FP	Fenestron <sup>®</sup> power, kW
FT	Fenestron <sup>®</sup> thrust, DaN
$h$	Radial position in the vein, m
$H$	Height of the vein, m
$h/H$	Normalized radial position
$k$	Turbulence kinetic energy, $\text{m}^2/\text{s}^2$
$Q$	Mass flow, kg/s
$p$	Static pressure, Pa
$p_\infty$	Ambient pressure, Pa
$R$	Shroud radius, m
$V_{\text{tip}}$	Blade tip velocity, $R\Omega$ , m/s
$V_z$	Axial velocity, m/s
$y^+$	Nondimensional wall distance
$\varepsilon$	Rate of turbulence kinetic energy dissipation, $\text{m}^2/\text{s}^3$
$\rho$	Density, $\text{kg}/\text{m}^3$
$\omega$	Frequency of turbulence kinetic energy, $\text{s}^{-1}$
$\Omega$	Rotation speed

## 1 INTRODUCTION

The Fenestron<sup>®</sup> was developed by the engineering department of Sud-Aviation (Airbus Helicopters) in 1970's [1,2] as an alternative solution to the conventional tail rotor. The principal function of the Fenestron<sup>®</sup> is to generate a thrust to counterbalance the torque of the main rotor. Improvements, in terms of safety and noise, for light-to-medium helicopters, have made it a trademark for Airbus Helicopters. The system is composed of a shrouded rotor and topped with a large vertical fin [3], as described in Fig. 1. The shroud includes a collector with

rounded lips, a cylindrical zone at the blade passage, and a conical diffuser. The gearbox (hub) is supported by three arms or a stator row and fairs systems which provide power to the rotor and control the blade pitch angle. The rotor pitch monitors the rotor thrust of the Fenestron<sup>®</sup>. In hover flight, the rotor leads the flow from the collector to the diffuser which creates the shroud effort. The thrust of the Fenestron<sup>®</sup> is thus composed by the shroud and the rotor thrusts.

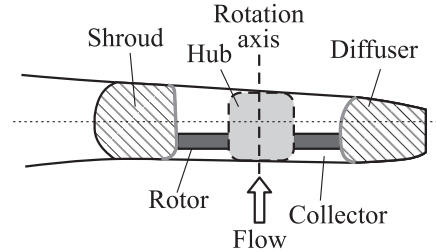


**Figure 1** Overview of the Fenestron<sup>®</sup> principle

The sizing of the Fenestron<sup>®</sup> is still a challenge due to the complexity of the flow. The internal flow of the Fenestron<sup>®</sup> is three-dimensional (3D), turbulent and, unsteady due to the interactions between fixed (shroud-stator) and rotating parts (rotor). Like in most turbomachines, secondary flows also exist in the Fenestron<sup>®</sup>, such as the tip leakage flow induced by the clearance between the rotor and the shroud. As a consequence, the analysis of the flow in realistic industrial configurations remains very difficult, even in a wind tunnel environment. Supported by experimental campaigns [1–6], a better understanding of the flow physics in these systems can be expected thanks to recent progresses in Computational Fluid Dynamics (CFD).

Several numerical approaches have been proposed in the literature to represent the flow in Fenestron<sup>®</sup> configurations. For example, the use of a two-dimensional (2D) axisymmetric model has been carried out on the Dauphin helicopter in hover flight, showing good agreement with the measurements [3]. However, this approach can be used only for axial flight conditions and 3D effects, such as blade tip vortices, are not represented. Another way to model the flow in the Fenestron<sup>®</sup> consists in solving Navier–Stokes equations on a 2D-axisymmetric shroud and by modeling the fan as a fully coupled, time-averaged momentum source term in the momentum equation [7]. While numerical predictions were in good agreement with measurements in the collector area, the pressure distribution was not accurately estimated in the blade region [7]. Other works reported in the literature suggest to use an approach based on a 3D geometry of the shroud [8–11]. The rotor is modeled by an actuator disk that uses the momentum and blade element theory to estimate the rotor thrust corresponding to a single pitch. The major benefit of the model is the computational cost reduction due to the rotor simplification. This approach allows computing the Fenestron<sup>®</sup> performance in the whole flight domain. However, this method does not represent 3D effects in the vicinity of the blade, such as tip clearance and blade swirl. It usually results in an unrepresentative local flow into the vein [11].

To improve the quality of the numerical predictions for 3D flows, the solution is thus to consider the full 3D domain with rotating (rotor) and fixed (shroud-hub-stator-fin) parts [12, 13]. The advantages of this method are the accuracy of the geometry and the possibility to perform all flight conditions. Unfortunately, this process remains time consuming in terms of both mesh generation and simulation time. To balance the simulation cost, it is possible to reduce the whole domain to a single blade passage with spatial periodic conditions [14]. This approach has been validated in hover flight on the EC135 geometry [13]. Despite the increase of the available computing power, only a few studies deal with the validation of the numerical method for 3D flows, as reported in [13]. The scope of this paper is thus to evaluate the influence of numerical parameters (mesh, scheme, and turbulence) on the global performance and local flows of the Fenestron<sup>®</sup> in hover flight.

To validate the method, numerical predictions are compared to bench test measurements on a full-scale Dauphin Fenestron<sup>®</sup> [3]. The CFD approach is based on the single blade passage proposed by Mouterde *et al.* in [14]. Since this work focuses on the local flow and interactions between the rotor and the shroud, the stator is not modeled in order to simplify the geometry. The numerical simulation of the flow relies on a representation of the 3D flow with a Reynolds-Averaged Navier–Stokes (RANS) approach (all turbulent scales are modeled). The first part of the paper details the experimental test case and computational setup. Then, the second part of the study proposes an evaluation of the meshing strategies. The Chimera technique is compared to a fully coincident meshing approach. For the Chimera technique, an evaluation of the meshing refinement is conducted. The third part of the paper proposes to evaluate the influence of numerical schemes and turbulence modeling on the prediction of the Fenestron<sup>®</sup> performance. The last part details an analysis of the flow in the blade tip region.

## 2 STUDY CASE

### 2.1 Experimental Case

The test case investigated in this paper is the Dauphin Fenestron<sup>®</sup> investigated by Morelli and Vuillet [3]. The experiments were carried out on a scale one test bench in hover flight. The measurements on the ducted rotor have been done to compare different rotor and shroud configurations. Among the different configurations described by Morelli and Vuillet [3], the reference case is chosen. It is based on a rotor with 11 equally spaced blades and a hub supported by three arms. A balance (with an accuracy of 1%) and a torque system (with an accuracy of 0.5%) are used to measure thrust and power. As illustrated in Fig. 2, the local flow is evaluated by measuring the static pressure with 32 steady sensors located

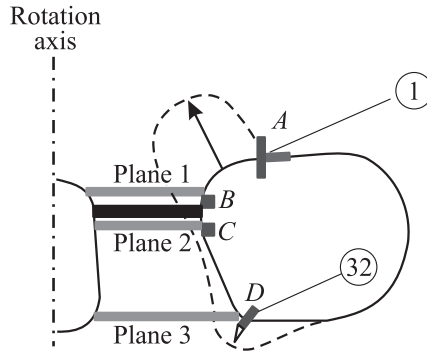


**Figure 2** Locations of static pressure measurements at the shroud (from [3])

along the duct vein. The flow is also characterized upstream (plane 1) and downstream (planes 2 and 3) the rotor at several radial locations with a 5-hole probe.

## 2.2 Computational Setup

The numerical simulations are performed with the code *elsA* developed by ONERA [15]. This solver is a multidisciplinary code object-oriented, specialized in both internal and external flows. This code solves both Euler and Navier–Stokes equations. It is based on a cell-centered finite volume formulation on multiblock structured meshes. A wide panel of turbulence models and numerical schemes is available. The study reported in this paper relies on a steady-state RANS approach. Boundary layers are assumed to be fully turbulent due to the large Reynolds number, based on the rotor chord ( $Re > 10^6$ ). As reported in [16], there are 4 main sources of errors when comparing numerical predictions with experimental data:

- (1) accuracy of the simulated geometry (and difficulty to represent small details such as technological effects);
- (2) boundary conditions (e. g., isothermal or adiabatic walls, far-field approximation);
- (3) adequacy between the numerical scheme (spectral properties of the scheme) and the mesh grid quality; and
- (4) turbulence modeling (RANS, Large Eddy Simulation (LES), etc.).

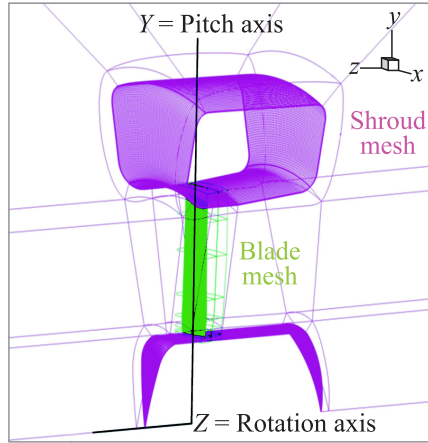


**Figure 3** Chimera grid assembly

This work specifically handles the two last sources of errors (discretization and turbulence modeling errors). To do this, different meshing approaches, numerical schemes, and RANS-based turbulence models are benched and their influence on the global performance and local flows predictions are evaluated. For all computations, a 3D single blade passage is chosen. Periodic conditions are applied on the lateral faces of the domain. Far-field boundary conditions are used for the external boundaries of the domain. The size of the domain is  $10R$  in each direction (with  $R$  being the radius of the shroud of the Fenestron<sup>®</sup>) around the shroud geometry. Previous simulations have been run with a  $20R^2$  box to check that the size of the domain has no influence on local flow and global performance predictions. Shroud, hub, and blade walls are represented with nonslip boundary conditions. The rotor rotates around the  $Z$ -axis and the blade pitch axis is defined as the  $Y$ -axis as shown in Fig. 3.

### 3 MESHING STRATEGY FOR FENESTRON<sup>®</sup> ISSUES

For structured multiblock meshes, the main difficulty lies on the grid generation process around complex geometries. Concerning the Fenestron<sup>®</sup>, the blade pitch variation  $[-10^\circ; +40^\circ]$  and the rotor tip clearance represent a considerable challenge for the grid topology and the mesh quality.

First, in order to choose the correct meshing strategy, the coincident approach is compared to the Chimera method. The coincident approach is the reference method to simulate with accuracy the geometry. Nevertheless, with a variation of  $50^\circ$  of pitch angle, a given grid topology is not adapted for all

blade pitches [13] (so, the meshing should be adapted to each blade pitch which is not affordable to describe the whole performance curve). The second meshing strategy is the Chimera method [11,17]. The advantage of the Chimera approach is to segregate the mesh generation of fixed and rotating parts. Nevertheless, the overset method induces conservation losses through the interpolations between meshes. Moreover, fixed and rotating cannot be fully encased without an overlapped grid or a gap between them. Then, the second part of the work proposes an evaluation of the grid refinement for the Chimera method. The aim is to compare four grid refinements to evaluate the influence on the performance of the Fenestron<sup>®</sup> and on the rotor wake dissipation. All calculations presented in this section are carried out with the two-equation turbulence model  $k-\omega$  of Kok [18] and a second-order centered numerical scheme [19]. The first study is carried out on the M1 grid (see Table 1 in subsection 3.4) with 6 million grid points.

### 3.1 Description of the Coincident Approach

Two strategies can be used for the meshing of the Fenestron<sup>®</sup> with a coincident approach. On the one hand, D'Alascio *et al.* [13] generated the grid topology for high pitches and encountered difficulties for low blade pitches. On the other hand, the work reported in this paper proposes to mesh in the first instance

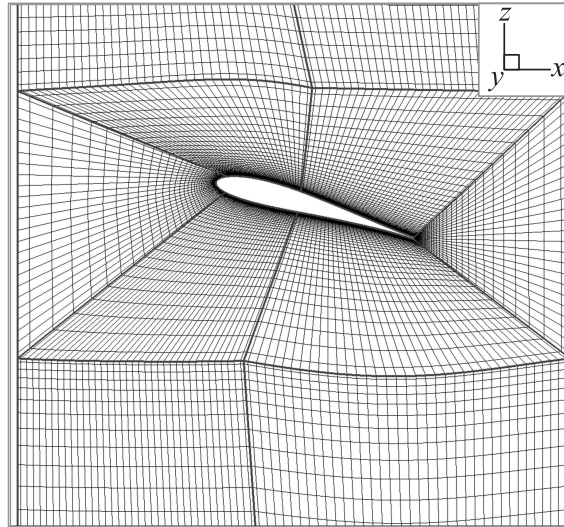


**Figure 4** Two-dimensional view of the rotor grid for the coincident approach at  $h/H = 0.85$

the low pitches and to adapt the grid topology for high pitch cases. An O-grid topology is used for the shroud, hub, and blade geometries. An H-topology is adopted for the blade tip area. The reference mesh is made of 156 blocks. The size of the first cell is imposed to achieve a normalized wall distance around unity ( $y^+ \sim 1$ ) which is mandatory to fully resolve boundary layers. The blade grid at 50% of the span is presented in Fig. 4 for a pitch of  $25^\circ$ .

### 3.2 Description of the Chimera Approach

For the Fenestron<sup>®</sup> application, the Chimera method consists in separately generating the blade and the shroud-hub meshes thus permitting to easily set up the pitch around the blade pitch axis, as shown in Fig. 3. The assembly of the two meshes is realized by the application of overlapping boundary conditions and masking conditions for areas corresponding to a solid. For both boundary conditions, the transfer of conservative and turbulent variables is done through 3D nonconservative interpolations. The Alternative Digital Trees (ADT) method [20] is used to solve the interpolation search cell procedure for fixed and rotating meshes. The second-order interpolation is chosen to improve the accuracy of the interpolation with a particular care for grid consistence between the two meshes. An evaluation of the conservative losses inherent to the Chimera technique is proposed in subsection 3.3. An encased problem is induced

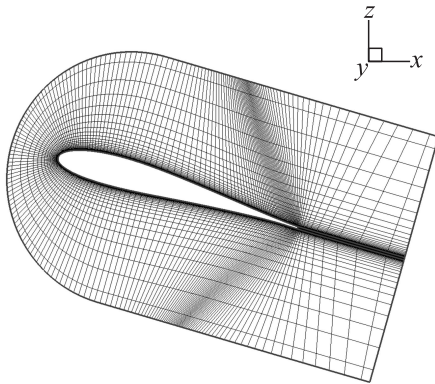


**Figure 5** Two-dimensional view of the rotor grid with the Chimera approach at  $h/H = 0.85$

by the Chimera approach, which results in a nonphysical root gap of a size similar to the shroud gap.

The grid topology for the rotor blade is based on a C-H topology around the blade profile, as presented in Fig. 5. Blade extremities (tip and root) are discretized by an H fluid volume topology. The first cell is set in order to obtain  $y^+ \sim 1$  at wall. The whole blade mesh contains 22 blocks, representing  $1.5 \cdot 10^6$  cells. The background mesh includes the shroud and the hub geometries. The grid generation is first done in two dimensions and is then extruded in a periodic 3D mesh. An O-block is chosen for the meshing of shroud and hub walls. The size of the first cell is also set to  $y^+ \sim 1$ . The whole background mesh is composed of 21 blocks and  $4.5 \times 10^6$  cells.

### 3.3 Comparison of the Two Strategies

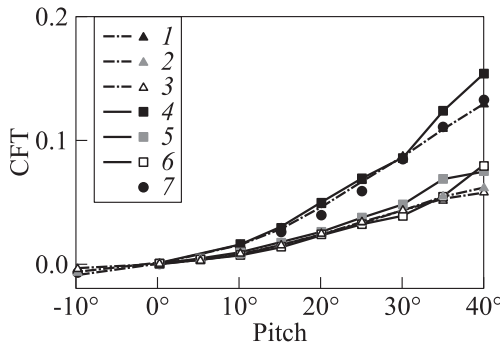
This part is dedicated to the comparison between the coincident approach and the Chimera technique. It is first proposed to evaluate the conservative losses of the Chimera method, as it is performed for turbomachinery [21]. To quantify the losses induced by the overset method, the mass flow difference  $\Delta Q$  is estimated from plane 1 (upstream the rotor) to plane 3 (downstream the rotor) as

$$\Delta Q = \frac{Q_{p1} - Q_{p3}}{Q_{p1}},$$

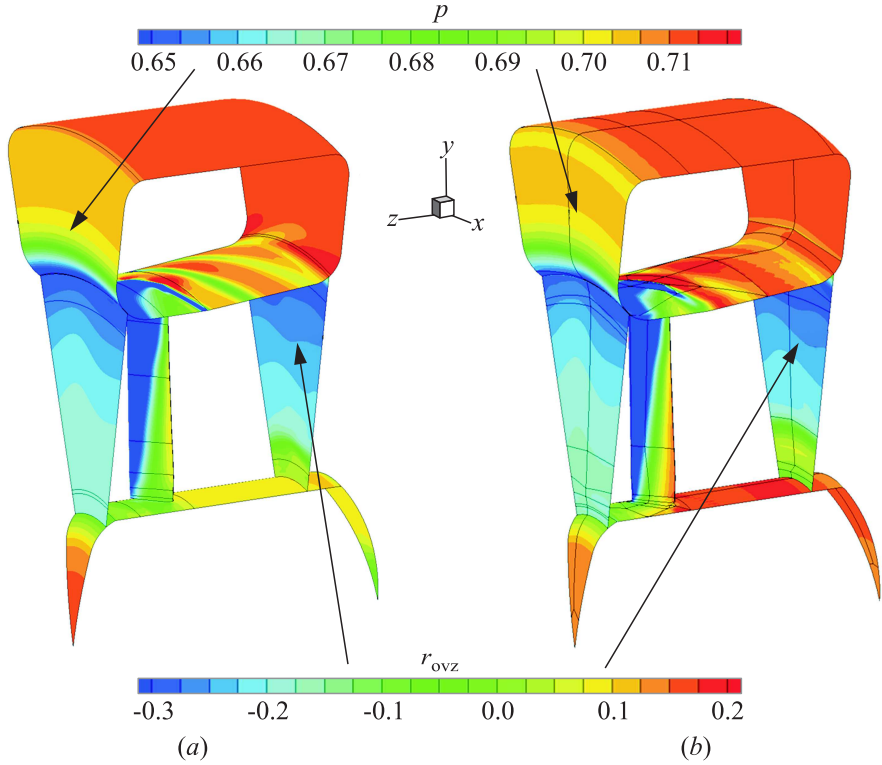
with  $Q$  being the mass flow. The mass flow difference is close to 1.0% for a grid of  $6 \cdot 10^6$  cells (grid M1). With the finest grid (grid M3,  $23 \cdot 10^6$  cells), the mass flow loss reduces to 0.1%.

Figure 6 compares the numerical predictions with the two strategies to the measurements. The global thrust as well as the shroud and the rotor thrusts are presented. According to the Froude theory [6], for both approaches, the total thrust of the system is the result of half rotor and shroud thrust as also reported in wind tunnel campaigns [4]. Until a blade rotor pitch of  $+30^\circ$ , the numerical predictions are not modified by the grid strategy. Then, from  $+30^\circ$  to  $+40^\circ$ , the coincident approach overestimates the Fenestron<sup>®</sup> thrust compared to measurements. This is related to an overestimation of the rotor thrust contribution.

For analyzing the influence of the grid strategy on the local flow, normalized static pressure on the shroud for blade pitch  $+35^\circ$  is presented in Fig. 7. In the collector area, the static pressure distributions are equivalent for both strategies. It is coherent with the shroud polar curves observed in Fig. 6. With the



**Figure 6** Comparison of the thrust coefficient between Chimera technique (1–3), the coincident approach (4–6), and measurements (7): 1 and 4 — Fenestron<sup>®</sup>; 2 and 5 — Rotor; and 3 and 6 — shroud



**Figure 7** Flow field for Chimera (a) and coincident (b) approaches for pitch  $35^\circ$

coincident approach, the static pressure distribution is affected by the mesh discretization in the vicinity of the blade (see Fig. 7b). As a consequence, periodic blade wakes more quickly dissipate compared to the Chimera approach due to the low-quality grid in the region of the shroud.

For the Chimera approach, Fig. 8 points out the dissipation of the rotor wake at the trailing edge due to the interpolation inherent to the method. With the coincident approach, the wake is not dissipated but the resolution of the flow around the leading edge is influenced by the mesh quality.

To conclude, the Chimera approach is better adapted than the coincident approach to describe the flow in a large range of blade pitches. To overcome this limitation, the coincident grid should be redesigned for each blade pitch which is a costly task if automatic adaptive grid methods are not available. At this step, the use of the Chimera approach is thus preferable.

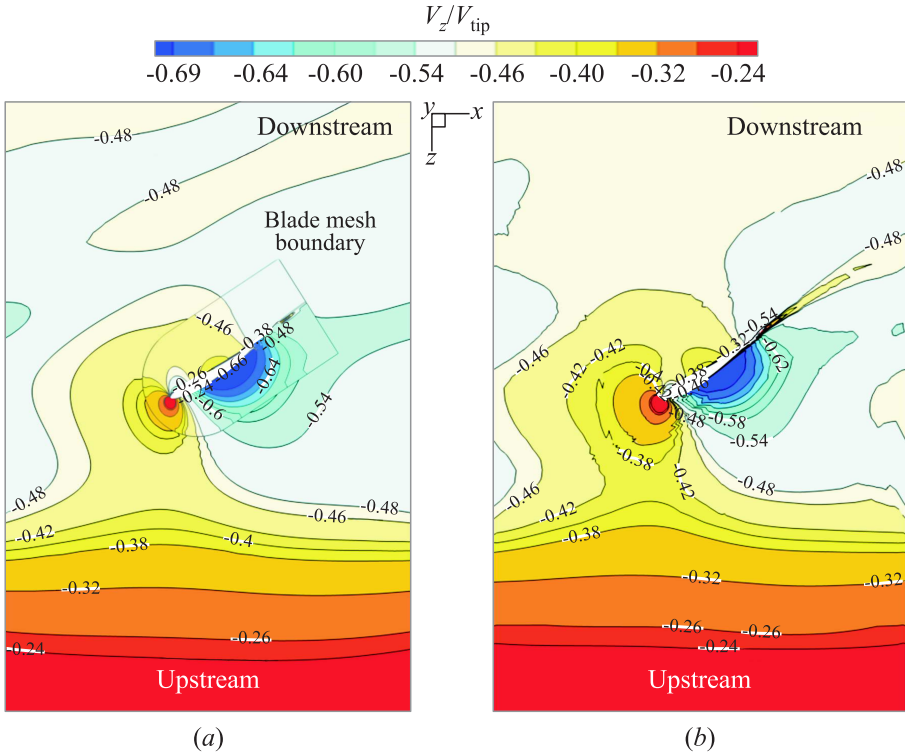


**Figure 8** Axial velocity isocontours at  $h/H = 0.85$  on Chimera (a) and coincident (b) approaches

### 3.4 Analysis of Grid Refinement

The effect of grid refinement is carried out for 4 different grids, from  $4 \cdot 10^6$  cells (grid M0) to  $23 \cdot 10^6$  cells (grid M3) as shown in Table 1. All computations in this section are performed with the two-equation turbulence model of Kok [18] with the Shear Stress Transport (SST) correction and a second order centered scheme [19].

**Table 1** Mesh grid refinement

Mesh	M0 (coarse)	M1 (reference)	M2 (intermediate)	M3 (fine)
Boundary layer (normal direction)	73	109	205	313
Vein (Z-axial direction)	82	123	255	395
Total mesh size (millions of points)	4	6	12	23

### 3.4.1 Global performance predictions

A comparison of the numerical predictions with the bench test is carried out in Figs. 9a and 9b. The higher the pitch, the more the performance prediction is sensitive to grid refinement. A coarse mesh overestimates the thrust at blade pitches higher than  $+35^\circ$ . A better grid refinement reduces the difference with the measurements.

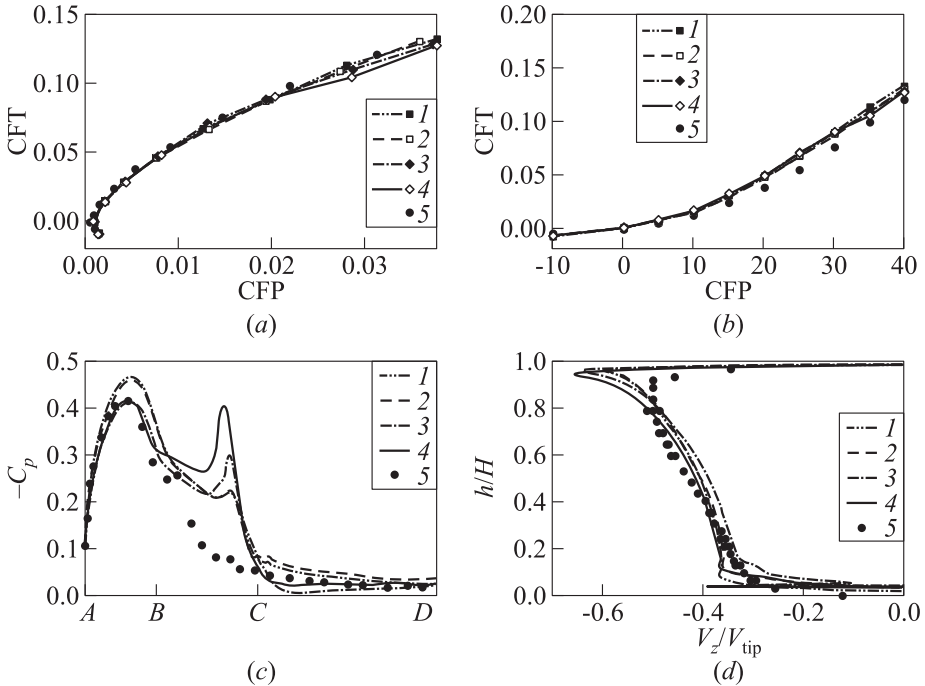


**Figure 9** Influence on global and local performance of the grid refinement (1 — grid M0; 2 — grid M1; 3 — grid M2; and 4 — grid M3) to measurements [3] (5): (a) Fenestron® CFT-CFP Polar; (b) Fenestron® CFT-Pitch Polar; (c) Pressure coefficient distribution on the shroud — pitch  $+35^\circ$ ; and (d) axial velocity distribution in the vein plane 2 — pitch  $+35^\circ$

### 3.4.2 Local performance predictions

The effect of the refinement is analyzed for a high blade pitch of  $+35^\circ$ . Figure 9c presents the pressure coefficient distribution through the vein (from the collector lip A to the diffuser lip D (see Fig. 2)). From point A to B, the upper collector zone evolves in a low-pressure area where the suction peak is reached at the

maximal curvature radius. This region of the shroud generates most of the thrust. Then, in the blade region, from point  $B$  to  $C$ , the decrease of the pressure is related to the presence of the blade tip vortices. This phenomenon will be better described in section 5. Through the diffuser, from point  $C$  to  $D$ , the pressure returns to the ambient static pressure value.

For all mesh refinements, numerical results and tests follow the same trend. The pressure on the collector is more sensitive to grid refinement than the rest of the flow. Only refinements above grid M1 are in good agreement with the measurements. The numerical simulations with grids M2 and M3 predict a stagnation zone at the end of the collector and before the blade passage. On the diffuser area, the solution is sensitive to the junction of the blade with the diffuser.

The grid refinement has also an influence on the pressure peak.

Figure 9d shows the radial profile of the axial velocity, extracted from plane 2, as a function of the radial position in the duct. Blade velocity distributions are

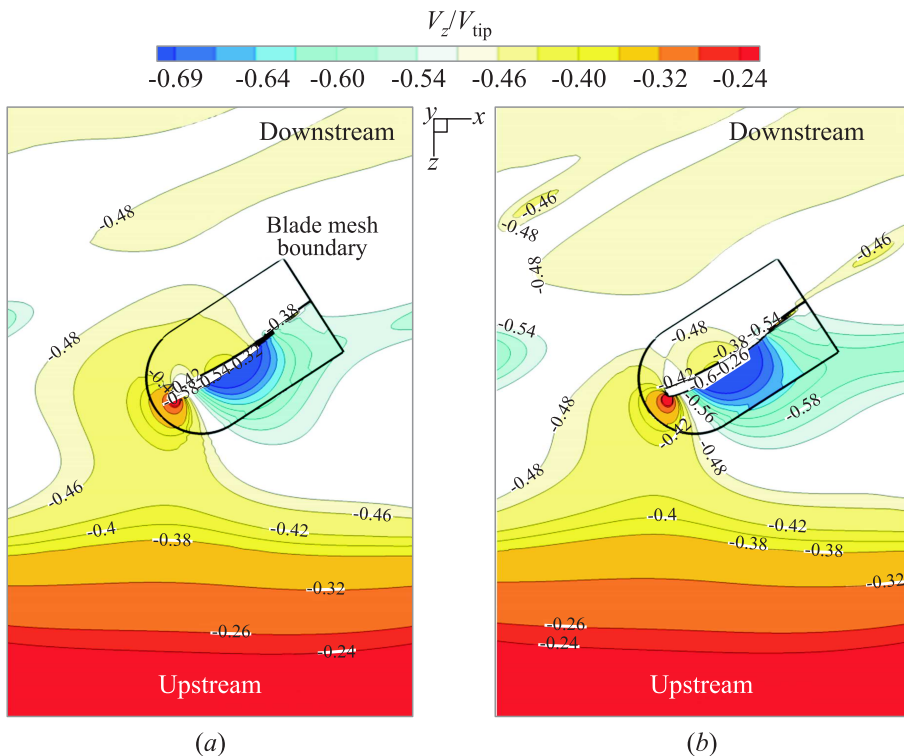


**Figure 10** Numerical comparison of axial velocity isocontours with  $h/H = 0.85$  between coarsed (a, M1) and refinement (b, M3) meshes

obtained using an azimuthal mass flow averaging. Three zones are underlined. The first zone, from  $h/H = 0$  to  $0.05$ , corresponds to the blade root region which is influenced by the nonphysical root leakage flow. The second one is the “linear zone” of the rotor, from  $h/H = 0.05$  to  $0.9$ . The third area  $h/H = 0.9$  to  $1$ , highlights the effect of blade tip vortices. In the linear zone, numerical predictions follow the same trend as the measurements. The axial velocity is overestimated at both the shroud and the root. In the blade tip region, axial velocity is overpredicted by 20% for the grid M0 to 30% for the grid M3. This observation is correlated with the suction peak that is discussed in section 5.

### 3.4.3 Effect on the rotor wake

Figure 10 presents the axial velocity at  $h/H = 0.85$  for the M1 and M3 grids at pitch  $+35^\circ$  (the solution of the blade grid is overlapped on the background grid) in order to show the wake dissipation. As expected, the wake dissipation is reduced with the finest grid (M3). This observation is in agreement with conservative losses described in subsection 3.3.

Therefore, to preserve the rotor wake, the mesh of the shroud (which is connected to the rotor grid through Chimera interpolations) should be refined by a factor 3 (compared to the coincident grid) in the radial direction.

## 4 NUMERICAL PARAMETERS

### 4.1 Influence of the Numerical Scheme

To complete the grid refinement study, the influence of the numerical scheme is estimated. Three classical numerical schemes are tested. The second-order centered scheme of Jameson, Schmidt, and Turkel (JST) [19] is compared with the second-order Advection Upstream Splitting Method Preconditioned (AUSMP) [22] and the third-order scheme of Roe [23]. To stabilize the JST scheme, an artificial viscosity term is added with a scalar artificial viscosity. The linear fourth-order dissipation term  $k_4$  is set to 0.016. All simulations presented in this section are conducted on grid M1 with the two-equation turbulence model of Kok [18]. Figure 11a shows the convergence of the numerical solution for the three schemes. The residual decreases by three orders of magnitude which is sufficient to consider that the convergence is achieved.

#### 4.1.1 Global performance predictions

The numerical power prediction is compared to experimental data in Fig. 11b. For a high level of thrust, the increase of the scheme order improves the power

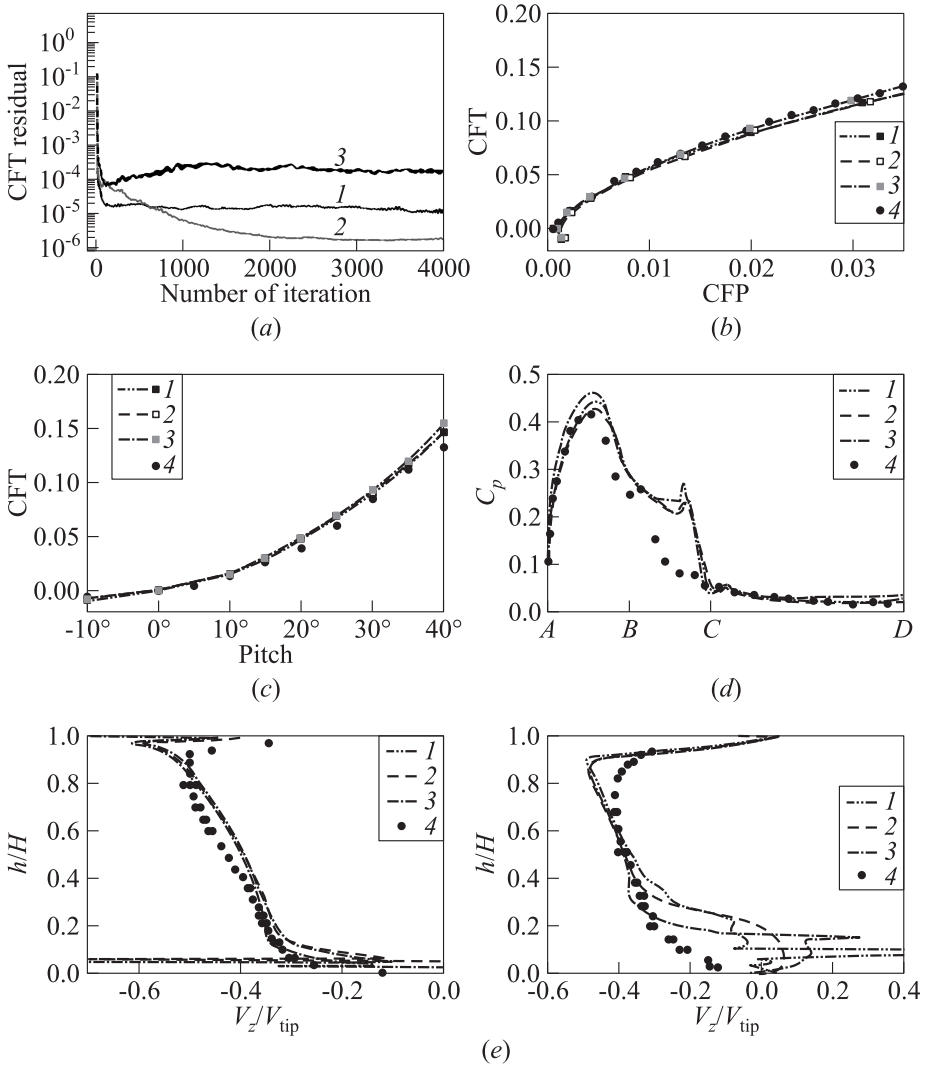


**Figure 11** Numerical comparison of convective scheme for reference mesh: 1 — JST 2nd order; 2 — AUSMP 2nd order; 3 — Roe 3rd order; 4 — experiments; (a) thrust convergence of the shroud; (b) Fenestron® CFT-CFP Polar; (c) Fenestron® CFT-Pitch Polar; (d) pressure coefficient distribution on the shroud — pitch  $+35^\circ$ ; and (e) axial velocity distributions in the vein plane 2 (left column) and plane 3 (right column)

estimation. However, on the thrust polar (Fig. 11c), the third-order scheme of Roe overestimates the thrust compared to experimental data. For high pitches, a balance is established between the accuracy of the power estimation, which needs a low dissipation from the numerical schemes, and the smoothing of the flow oscillations to reach the correct rate of thrust.

#### 4.1.2 Local performance predictions

Figure 11d presents the coefficient of pressure as a function of the vein distance for a blade rotor pitch of  $+35^\circ$ . On the collector area, the pressure distribution is very sensitive to the numerical scheme. The JST scheme is in good agreement with the experimental bench data while the third-order scheme overestimates the static pressure coefficient at this location in agreement with the polar results. Through the blade zone (from  $B$  to  $C$ ) and in the vicinity of the diffuser, the solution is not sensitive to the numerical scheme. Figure 11e (left column) presents the axial velocity distribution on plane 2 for a blade rotor pitch of  $+35^\circ$ , in the vein. The solution is not sensitive to the numerical schemes in the linear zone and in the vicinity of the blade tip. Indeed, the overprediction of the velocity deficit in the tip region should not be attributed to the grid/scheme combination. Actually, most discrepancies are observed in the blade root region as shown in Fig. 11e (right column) at plane 3.

A qualitative study of the blade tip region has been conducted for blade rotor pitch  $+35^\circ$ . The Q-criterion [24] is taken positive to point out the blade tip vortices as illustrated in Fig. 12. Firstly, for the three schemes considered, the blade tip roll-up has the same trend. A roll-up appears from the trailing edge and is separated from the blade tip at the middle of the chord. Secondly, the convection of the blade tip vortex is influenced by the order of the schemes. The mechanism is related to the creation of a “mirror vortex” described by Cerra

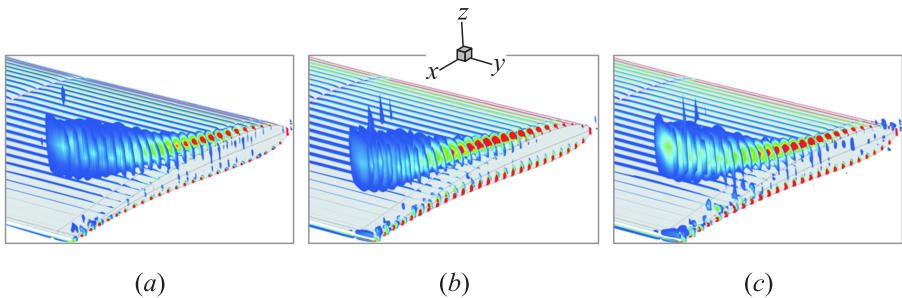


**Figure 12** Comparison of  $Q$  positive function on the blade tip for different numerical schemes: (a) AUSMP 2nd order; (b) Jameson 2nd order; and (c) Roe 3rd order

and Smith [25]. The wall (the shroud) induces the generation of a secondary vortex, rotating in the opposite direction. The results suggest that the third-order scheme transports the tip vortex further downstream than the second-order schemes. Therefore, the interaction between the blade vortex flow and the shroud is affected by the numerical scheme. The third-order scheme preserves the Q-criterion farther the blade tip than the second-order schemes.

## 4.2 Influence of Turbulence Modeling

The turbulence modeling is a key issue in RANS-based simulations. Different first-order turbulence models are compared in this section: the one transport equation model of Spalart–Allmaras (S–A) [26] is compared with the two transport equations model of  $k$ – $\varepsilon$  (Launder–Sharma (L–S)) [27] and  $k$ – $\omega$  (Kok [18] and Menter [28]) with SST correction. The SST correction proposed in [29] avoids the delay in the prediction of adverse pressure gradient effects. This correction should thus be helpful for the flow prediction at high pitch angles, for which the adverse pressure gradient is more important. All simulations presented in this section are performed on grid M1 with the second-order centered JST scheme. Figure 13a shows the convergence of the numerical solution with the four turbulence models. The residual drops by 3 or 4 orders of magnitude.

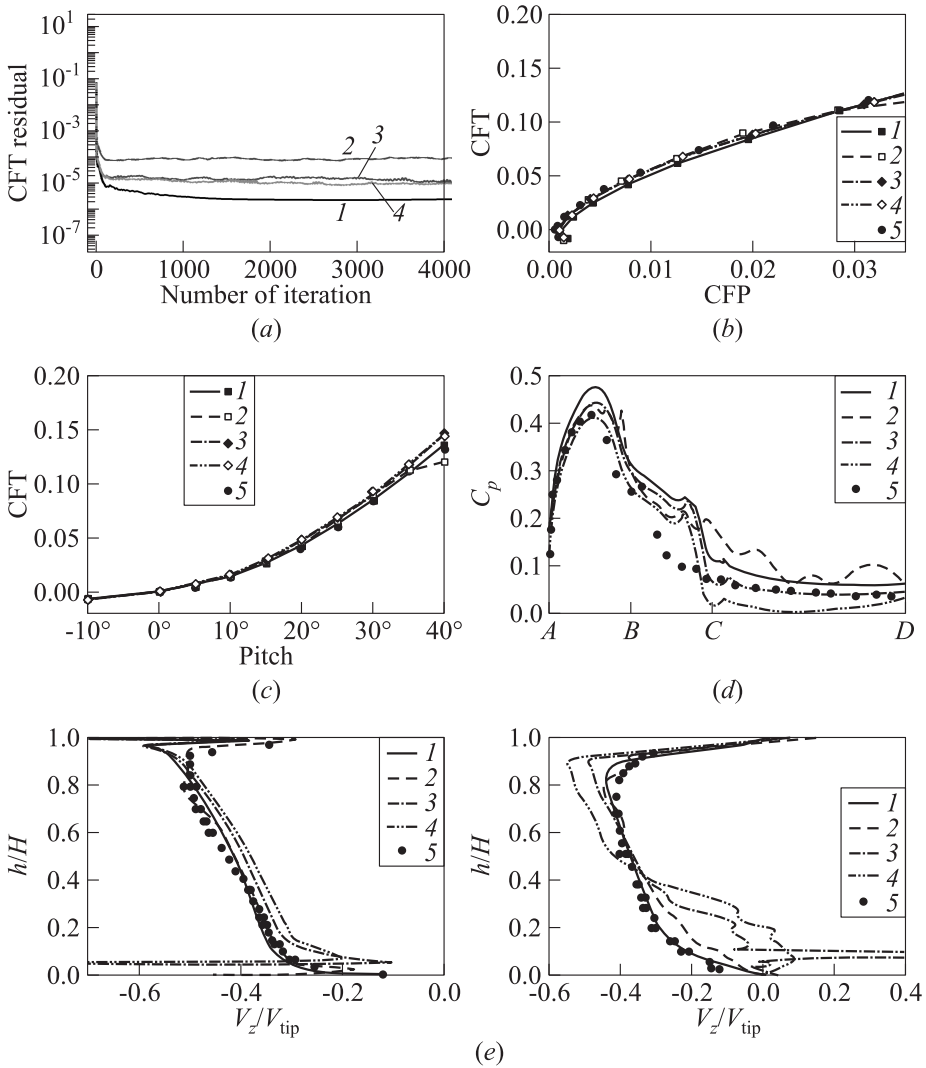
### 4.2.1 Global performance prediction

Figure 13b presents the power estimation depending on the turbulence modeling. In comparison with the experimental data, the thrust-power polars predicted by the Menter and Kok models overestimate the thrust at a high blade pitch angle. The S–A model reveals to be extremely dissipative.

The thrust polar shown in Fig. 13c highlights two zones in comparison with the measurements: the first zone which is linear and corresponds to low pitch angles  $[-10^\circ; +35^\circ]$  and the second zone which corresponds to high pitch angles  $[+35^\circ; +40^\circ]$ . In the linear zone, the two transport equation models (L–S, Kok, and Menter) overestimate the thrust predictions compared to the S–A model. The differences increase at high blade rotor pitch. The L–S model predicts a region of stalled flow earlier compared to other models.

### 4.2.2 Local performance predictions

An analysis of the local flow is carried out on the blade rotor pitch angle of  $+35^\circ$ . Pressure coefficient distributions at the shroud are presented on Fig. 13d. From point *A* to point *B*, at the inlet lip, turbulence models have an important influence on the pressure peak predictions as shown in Table 2. The best agreement



**Figure 13** Numerical comparison of turbulence modeling for reference mesh: 1 — S-A; 2 —  $k-\epsilon$  L-S; 3 —  $k-\omega$  Kok; 4 —  $k-\omega$  Menter; 5 — experiments; (a) thrust convergence of the shroud; (b) Fenestron<sup>®</sup> CFT-Pitch Polar; (c) Fenestron<sup>®</sup> CFT-Pitch Polar; (d) pressure coefficient distribution on the shroud — pitch +35°; and (e) axial velocity distributions in the vein plane 2 (left column) and plane 3 (right column)

**Table 2** Relative errors between turbulence models and measurement for a blade rotor pitch angle of  $+35^\circ$  in part *A* to *B* of the shroud

Error, %	S-A	$k-\omega$ Menter	$k-\omega$ Kok	$k-\varepsilon$ L-S
$-C_p$	14	2	6	6

with measurements is observed with the  $k-\omega$  model of Menter (error is 2% with respect to the measurements).

A secondary increase of the coefficient of pressure is observed with the L-S model, close to point *B*, which does not appear in measurements and with other turbulence models. Figure 14 presents the axial velocity through the blade passage, from *B* to *C* for the L-S and Kok models. For the L-S model, a stall region appears before the blade position which is correlated to the distribution of the coefficient of pressure. However, all turbulence models show an increase of the pressure coefficient between points *B* and *C*, related to the tip clearance vortex which is observed in Fig. 14*b*.

Figure 13*e* (left column) shows the radial profiles of the normalized axial velocity downstream the rotor (plane 2). The magnitude of the axial velocity is overestimated by most of turbulence models (except the L-S model) compared to measurements, in the tip region (by about 20% with S-A and  $k-\omega$  models).

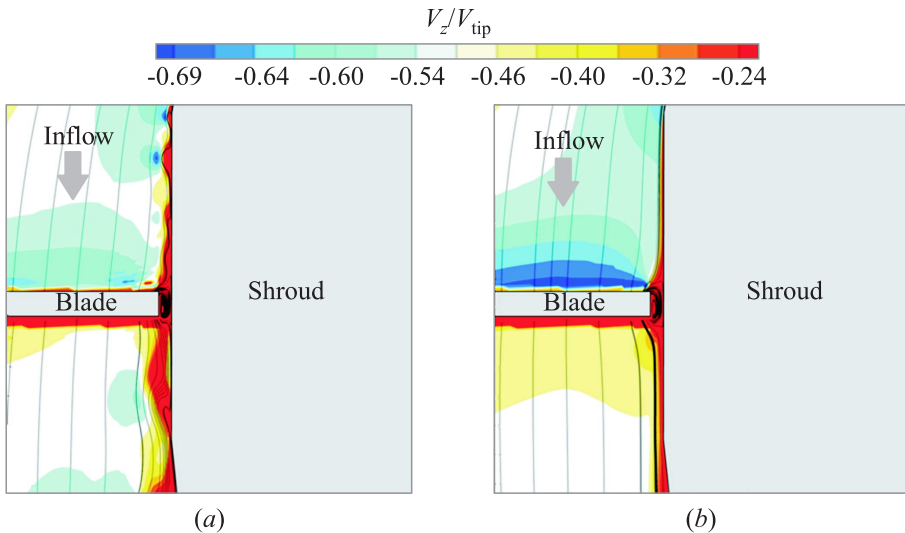


**Figure 14** Axial velocity distribution for different turbulence modeling: (a)  $k-\varepsilon$  L-S; and (b)  $k-\omega$  Kok

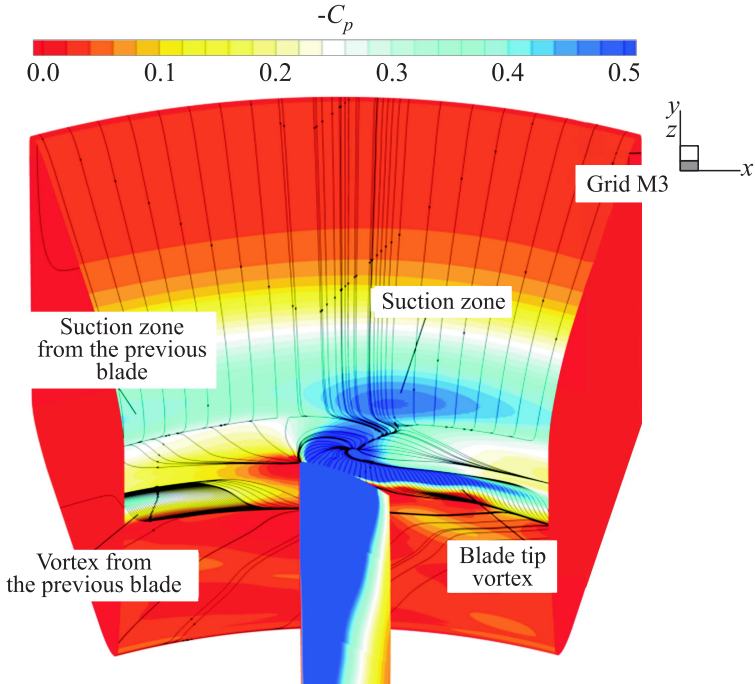
This observation underlines the difficulty for first-order turbulence models to accurately describe turbulence in the vicinity of the tip clearance. In the linear zone,  $h/H = 0.05$  to  $0.9$ , all turbulence models predict the same trend. At the blade root,  $k-\varepsilon$  and  $k-\omega$  models are more influenced by the root leakage flow than other turbulence models. The S-A predicts a higher level of turbulent kinetic energy than other turbulence models, resulting in an increase of the turbulent viscosity. This behavior limits the nonphysical root tip flow, which helps to match the measurements (however, not for the good reasons).

Figure 13e (right column) shows the radial profiles of axial velocity distribution in the diffuser (plane 3). The differences between turbulence models predictions are more important at this section than at plane 2. The main reason comes from the influence of the size of the stalled flow that is predicted at plane 2, which induces a redistribution of the axial velocity inside the vein. As for the prediction of the flow in the tip region at plane 2, it shows the difficulty to accurately predict the flow in such a configuration when separation occurs at high blade pitches.

This section shows that the global performance of the Fenestron<sup>®</sup> is sensitive to both numerical scheme and turbulence modeling. The power prediction is more influenced by the numerical schemes while the thrust is more influenced by the turbulence modeling. For local performance, the turbulence modeling is of paramount importance in the vicinity of the blade tip clearance.

## 5 ANALYSIS OF THE FLOW AT THE BLADE TIP REGION

In this section, the  $k-\omega$  model of Kok and the second centered order scheme of Jameson are used. The finest grid M3 is chosen ( $23 \cdot 10^6$  cells) to conduct the local flow analysis in the vicinity of the blade. Most discrepancies between numerical predictions and measurements appear in the blade passage (from point *B* to point *C*). In this region, two flow mechanisms interact. First, the blade tip vortex is generated by the tip clearance, close to the shroud. Then, the boundary layer of the shroud interacts with this vortex, leading to the secondary flow. This shear flow affects the tip region performance by promoting a 3D separation [30]. Figure 15 presents a 3D view of the pressure coefficient showing the effect of the blade tip vortex. The boundary layer of the shroud is sucked by the blade tip vortex; therefore, a suction peak appears in the coefficient of pressure (Fig. 16). Such a suction peak has already been reported in [7]. In general, the 3D flows are known to be challenging both for experimental sensors and numerical simulations; so, it can explain, at least partially, the discrepancies between numerical simulations and measurements. However, since this part of the shroud is parallel to the streamwise flow, it does not affect the shroud thrust.



**Figure 15** Distribution of the coefficient of pressure on the Fenestron® for grid M3 — pitch +35°

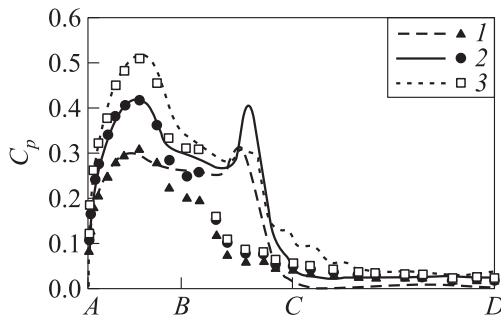


**Figure 16** Distribution of the coefficient of pressure on the shroud for several pitches (curves refer to calculations and signs to experiments): 1 — pitch 35° – eps; 2 — 35°; and 3 — pitch 35° + eps

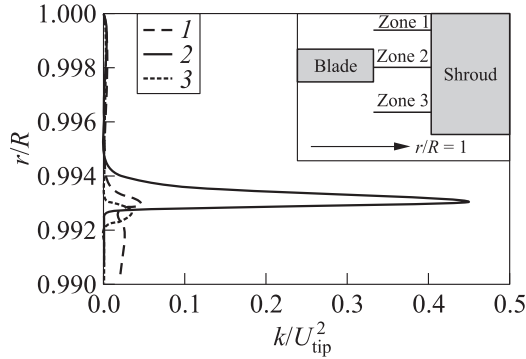


**Figure 17** Turbulent kinetic energy along the blade tip clearance for the  $k-\omega$  Kok model: 1 — zone 1; 2 — zone 2; and 3 — zone 3

In order to highlight the difficulty to simulate the flow in the blade region, two pitches around the blade pitch angle of  $+35^\circ$  are studied. “eps” refers to a small variation of a degree around the reference blade pitch angle of  $+35^\circ$ . Figure 16 presents the distribution of the pressure coefficient for three different pitches. The pressure coefficient distribution is well captured at three pitch angles compared to measurements. Thereafter, the behavior of the suction peak in the blade region depends on the blade pitch angle. The higher the pitch angle, the less the suction peak in the blade region. Moreover, the pressure coefficient before the blade passage and after the collector depends also on the blade pitch angle.

Figure 17 presents the turbulent kinetic energy along the cylindrical part of the shroud for the blade rotor pitch angle of  $+35^\circ$ . Three zones are plotted; zone 1 and zone 3 are extracted at 6% of blade chord before and after the blade, respectively, and zone 2 is extracted at the middle of the blade position. As expected, a peak of turbulent kinetic energy is observed at zone 2, which is related to the tip clearance flow. However, zone 1 reveals also a peak of turbulent kinetic energy (upstream the blade passage) due to the shroud boundary layer.

Figure 18 shows the flow field colored with the axial velocity for three blade pitch angles in the cylindrical part. Correlated with the pressure coefficient (see Fig. 15), three zones are highlighted: (i) a large velocity area in the collector region (which participated to the shroud thrust); (ii) a backflow that develops upstream the blade for blade pitch angle of  $+35^\circ - \text{eps}$  and  $+35^\circ$ ; and (iii) the tip clearance flow. The behavior of the backflow zone is sensitive to the blade pitch angle. Above a blade pitch angle of  $+35^\circ$ , the axial velocity imposed by the rotor becomes sufficient to delay the separation zone upstream the blade (see Fig. 18c).



and an overlapping approach (Chimera method). While the coincident method avoids the use of interpolations between grids of different density, it reaches quality limits for high pitch angles. An overdissipation is observed at such flow conditions due to the stretching of the mesh. In that regard, the use of the Chimera approach helps to overcome this difficulty.

If a sufficient care is brought to the grid, most numerical parameters do not influence the prediction of the Fenestron<sup>®</sup> performance until the blade pitch +35°. Beyond this pitch, discrepancies appeared. On the pressure distribution, the prediction of the collector area is influenced by the grid refinement and the numerical scheme. For high pitch angles, the turbulence modeling has also a major effect on the flow prediction. This is related to the difficulty for a RANS-based approach to tackle with complex flow phenomena such as boundary layers separations.

Some discrepancies are observed between numerical predictions and measurements, especially in the vicinity of the tip region and at high pitch angles (where flow separations are observed). A dependence of the flow solution to a small variation of the blade pitch angle exists at such high blade pitches. A separated zone upstream the blade is observed for blade pitch angle until +35°. Nevertheless, this work has shown that these errors cannot be attributed to the grid quality or the numerical scheme. The choice for the turbulence model has a large influence on the flow prediction.

As a perspective to this work, unsteady RANS and LES will be carried out on this configuration to better understand the role of flow unsteadiness and turbulence and to provide data about turbulence properties in the vicinity of the tip clearance.

## REFERENCES

1. Mouille, R., and G. Bourdaquez. 1970. Helicopter steering and propelling device. Patent 1.511.006.
2. Mouille, R. 1979. Ten years of Aerospatiale experience with the Fenestron and conventional tail rotor. *35th Annual National Forum of the American Helicopter Society*. Washington, DC.
3. Morelli, F., and A. Vuillet. 1986. New aerodynamic design of the Fenestron<sup>®</sup> for improved performance. *12th European Rotorcraft Forum*. Amsterdam, Netherland.
4. Morelli, F., and A. Vuillet. 1982. Le Fenestron<sup>®</sup> sur l'hélicoptère. *19ième Colloque d'aérodynamique appliquée*. Marseille, France.
5. Benek, J. A., J.L. Steger, and F.C. Dougherty. 1993. A Chimera grid scheme. *ASME Mini-Symposium on Advances in Grid Generation*. Houston, TX.
6. Leishman, J. G. 2002. *Principles of helicopter aerodynamics*. Cambridge University Press. 321–323.

7. Rajagopalan, R. G., and C. N. Keys. 1993. Detailed aerodynamic design of the RAH 66 FANTAIL USING CFD. *American Helicopter Society 49th Annual Forum Proceedings*. St. Louis, MI.
8. Alpman, E., L. N. Long, and B. D. Kothmann. 2003. Unsteady RAH-66 Comanche flowfield simulations. *American Helicopter Society 59th Annual Forum*. Phoenix, AZ.
9. Alpman, E., and L.,N. Long. 2003. Toward a better understanding of ducted rotor antitorque. AIAA Paper No. 2003-4231.
10. Cao, Y., and Z. Yu. 2005. Numerical simulation for turbulent flow around helicopter ducted tail rotor. *Aerosp. Sci. Technol.* 9:300–306.
11. Gardarein, P., S. Canard, and J. Prieur. 2006. Unsteady aerodynamic and aeroacoustic simulations of a Fenestron<sup>®</sup> tail rotor. *62nd American Helicopter Society*. Phoenix, Arizona, USA.
12. Lee, H. D., O. J. Kwon, and J. Joo. 2003. Aerodynamic performance analysis of a helicopter shrouded. *The 5th Asian Computation Fluid Dynamics*. Busan, Korea.
13. D’Alascio, A., F. Le Chuiton, E. Mouterde, L. Sudre, S. Kirstein, and H.-P. Kau. 2008. Aerodynamic study EC135 FEN HFC By means CFD. *American Helicopter Society 64th Annual Forum*. Montréal, Canada.
14. Mouterde, E., L. Sudre, A. M. Dequin, A. D’Alascio, and P. Haldenwang. 2007. Aerodynamic computations of isolated Fenestron<sup>®</sup> in hover conditions. *33th European Rotorcraft Forum*. Kazan, Russia.
15. Cambier, L., S. Heib, and S. Plot. 2013. The Onera elsA CFD software: Input from research and feedback from industry. *Mech. Ind.* 14(3):159–174. doi:10.1051/meca/2013056.
16. Denton, J. 2010. Some limitations of turbomachinery CFD. *ASME Turbo Expo 2010: Power for Land, Sea, and Air*. Vol. 7: Turbomachinery. Parts A, B, and C. Glasgow, U.K. 735–745.
17. Benoit, C., G. Jeanfavren, and E. Canonne. 2005. Synthesis of ONERA Chimera method developed in the frame of CHANCE program. *31st European Rotorcraft Forum*. Florence, Italy.
18. Kok, J. 1999. Improvements of the two equation turbulence models in multi-block flow solvers: Free-stream dependancy and transition. Rapport technique, AVTAC/TR/NLR/JCK990520/Draft2.
19. Jameson, A., W. Schmidt, and E. Turkel. 1981. Numerical solution of the Euler equations by finite volume methods using Range Kutta time-stepping schemes. AIAA Paper No. 198-1259. doi: 10.2514/6.1981-1259.
20. Bonet, J., and J. Peraire. 1991. An alternating digital tree (ADT) algorithm for 3D Geometric searching and intersection problems. *Int. J. Numer. Meth. Eng.* 31:1–17.
21. Castillon, L., G. Billonnet, S. Péron, and C. Benoit. 2010. Numerical simulations of technological effects encountered on turbomachinery configurations with the Chimera technique. *27th Congress (International) of the Aeronautical Sciences*.
22. Liou, M.-S., and J.-R., Edwards. 1999. AUSM schemes and extensions for low Mach and multiphase flows. *30th Computational Fluid Dynamics*. 1999-03 Von Karman lecture ser.

23. Roe, P. L. 1981. Approximate Riemann solvers parameters vectors, and difference schemes. *J. Comput. Phys.* 43(2):357–372.
24. Jeong, J., and F. Hussain. 1995. On the identification of a Vortex. *J. Fluid Mech.* 285:69–94. doi: 10.1017/S0022112095000462.
25. Cerra, A. W., and C. R. Smith. 1983. Experimental observations of vortex ring interaction with the fluid adjacent to a surface. Report FM-4. Department of Mechanical Engineering and Mechanics, Lenigh University.
26. Spalart, P. R., and S. R. Allmaras. 1992. One-equation turbulence model for aerodynamic flows. AIAA Paper No. 91-439.
27. Launder, B. E., and B. I. Sharma. 1974. Application of the energy dissipation model of turbulence to the calculation of flows near a spinning disk. *Lett. Heat Mass Transf.* 1:131.
28. Menter, F. R. 1992. +Improved two equation  $k-\omega$  turbulence models for aerodynamic flows. Technical Report NASA. Technical Memorandum 103975(1992).
29. Menter, F. R. 1993. Zonal two equation  $k$ -omega turbulence models for aerodynamic flows. AIAA Paper No. 93-2906.
30. Peacock, R. E. 1981. Blade tip gap effects in turbomachines: A review. Washington, DC: Naval Air Systems Command.